Ray tracing and FMC simulation in curved composite structures

Cite as: AIP Conference Proceedings **2102**, 130003 (2019); https://doi.org/10.1063/1.5099853
Published Online: 08 May 2019

Callum Lanherne, and Paul Wilcox

Ray Tracing and FMC Simulation in Curved Composite Structures

Callum Lanherne[1] and Paul Wilcox[2,a)]

[1]*Advanced Composites Collaboration for Science and Innovation (ACCIS), University of Bristol, Bristol, UK*
[2]*Ultrasonics and NDT Research Group, Department of Mechanical Engineering, University of Bristol, Bristol, UK*

[a)]Corresponding author: p.wilcox@bristol.ac.uk

Abstract. Composite materials present many challenges for the NDE community. Addressed here is the phenomenon of ray bending due to the introduction of curvature into anisotropic materials, using Dijsktra's algorithm for tracing rays. The influence of several important parameters is identified, and Dijkstra's algorithm is applied to calculating TFM focal laws in both simulated and experimental data. In both cases, an improvement in image quality is observed.

INTRODUCTION

Composite materials present interesting challenges for non-destructive evaluation. In this paper one particular problem is addressed: that of ray bending in inhomogeneous anisotropic media.

Rays are the energy trajectory of ultrasound. Ray theory (also known as geometric acoustics) is a high frequency approximation, requiring that:

$$\lambda << L, \tag{1}$$

where λ is the wavelength of interest, and L is the length scale of the system.

Ray bending occurs as a result of Fermat's principle [1, 2]. This is the statement that the energy path taken by ultrasound is the path of least time. Long fibre reinforced composites such as carbon fibre reinforced polymers (CFRPs) are inherently anisotropic, and when curved (for example in a corner section) the fastest paths are no longer straight lines. This is important for locating and sizing of discontinuities, as most methods involve a mapping of time signals onto spatial locations. When the ray path is not straight, this is a non-trivial matter.

A method that has been used previously on similar problems is the application of Dijkstra's algorithm to a discretised domain representing the medium under inspection. This has most widely been studied in geophysics [3], but has seen some interest in NDE [4]. In this paper the accuracy of Dijkstra's algorithm is inspected for CFRP, and its application to the total focussing method using full matrix capture (FMC) is investigated.

DIJKSTRA'S ALGORITHM

Dijkstra's algorithm (DA) is a single-source shortest path algorithm on a graph [5]. Here, a graph is defined as a set of vertices connected to each other via weighted edges, representing ultrasonic travel time along the straight edge. Given a starting node, DA finds the shortest path to any set of destination nodes. Segments of the ray are approximated by the straight edges of the graph; the weight is calculated by assuming a constant velocity on the edge, calculated from the local velocity and angle at the midpoint of the edge.

To apply this to the solution of Fermat's principle, several parameters must be considered:

- Vertex density
- Vertex connectivity
- Vertex distribution

45th Annual Review of Progress in Quantitative Nondestructive Evaluation, Volume 38
AIP Conf. Proc. 2102, 130003-1–130003-7; https://doi.org/10.1063/1.5099853
Published by AIP Publishing. 978-0-7354-1832-5/$30.00

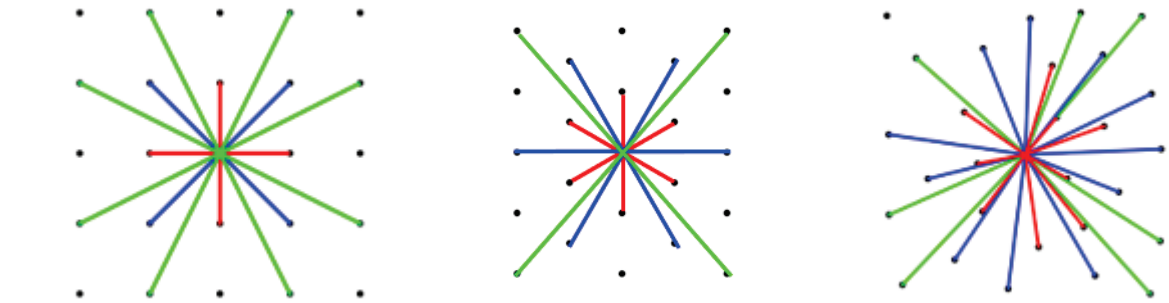

FIGURE 1. Different sampling methodologies. a) square grid sampling, b) hexagonally close packed sampling and c) Poisson disc sampling. Line demonstrate the number of unique angles that occur for given edge lengths (red, blue and green in order of increasing length).

Vertex density is the number of vertices per unit area. The higher the density, the better the approximation to the continuous medium. Thus, this parameter decision is simply a balance of accuracy versus computational time.

Vertex connectivity is somewhat more complex; it is important to have a sufficiently high angular resolution so that the straight line segments that approximate the continuously curved ray path are good approximations. High connectivity is therefore advantageous. However, high connectivity leads to potentially longer straight segments, which may compromise the accuracy of the approximation. These paths may be faster, but would be non-physical due to the averaged material properties in the ray segment. As such, a balance between angular resolution and path resolution must be found.

Vertex distribution is another important factor. Loosely defined, this how evenly distributed the vertices are, both translationally and rotationally. An example of an even translational distribution that is unevenly rotationally distributed is a regular square grid. An example of an even rotational distribution with uneven translational distribution (due to Poisson clumping) is a random distribution.

METHODOLOGY

Arrival time accuracy

In order to investigate the accuracy of Dijkstra's algorithm, a test model was devised. The specimen is a circular cross section of CFRP with concentric ply structure. The material properties vary smoothly in the azimuthal direction. This can be thought of as a pipe with zero inner radius. For first arrival times, this acts as a somewhat general solution. As long as ray theory is appropriate by Equation 1, the results should scale for any cylindrical CFRP component, with arbitrary inner and outer radius. The geometry is shown in Figure 2a).

The arrival times were first calculated by running a finite element simulation in Pogo FEA [6], which is a GPU optimised elastodynamic explicit finite element package, using a 2D triangular element mesh generated using Abaqus CAE. The input signal is a five cycle Hanning windowed sinusoid, with a centre frequency of 5 MHz, exciting a point source on the surface, shown in Figure 2a). A target mesh size of 15 μm was used to provide approximately 39 elements per wavelength at the peak frequency and slowest sound speed in the material. The specimen is unidirectional CFRP with no resin layers; the local material properties are given in Table 1. Arrival times were calculated throughout the specimen using an empirical threshold of -80 dB.

Before applying DA to the problem of ray tracing, there are several steps to complete. Firstly, the domain needs to be sampled. There are many ways to do this; in this paper, square grid sampling, hexagonal close packing (two

TABLE 1. CFRP material properties in local coordinate system

E_x (GPa)	E_z (GPa)	G_{xz} (GPa)	ν_{xz}	Density (kg m^{-3})
161	11.4	5.17	0.32	1600

orientations) and Poisson disc sampling are considered, shown in Figure 1. The input parameters for this step are the domain shape and the vertex density.

Secondly, the connectivity must be determined. This is defined by an allowable maximum edge length, r_{hop}, which is here called the hop radius. Three different hop radii are shown in Figure 1.

Finally, the edge weights must be found. This is achieved by calculating the angle-dependent velocity at the midpoint of each edge. By using the midpoint, reversibility of the ray paths is ensured.

Once these three steps are complete, DA can be used to calculate arrival times at each vertex. In this case, DA takes the sparse connectivity matrix as an input, and returns an arrival time for each vertex, and a list of vertex indices representing the previous vertex in the path.

Simulated contact FMC

FMC data was simulated using Pogo FEA [6]. A 64-element array was simulated by exciting the surface of the specimen with a 5-cycle Hanning windowed sinusoid, with a centre frequency of 5MHz. The specimen modelled is a 2D plane strain pipe cross section, shown in Figure 2b). Plies were modelled individually with a 64 ply quasi-isotropic layup $[(+45,\ 90,\ -45,\ 0)_8]_s$. 15 μm inter-laminar resin layers are assigned isotropic epoxy material properties. The total ply thickness (homogenised ply + inter-laminar layer) is 0.25 mm. The defect is a 5 mm flat-bottomed hole, penetrating 6 mm into the concave surface of the pipe section.

Experimental immersion FMC

To obtain experimental data, a composite corner section with a 5mm flat bottomed hole drilled 6 mm into the concave surface was inspected in immersion, shown in Fig. 2c). A 128 element array with centre frequency of 5MHz was used.

To generate images for the simulated and experimental data, the total focussing method was used, defined by

$$I(x,z) = \sum_i \sum_j s_{ij}(\tau(x,z)) \tag{2}$$

where $I(x,z)$ is the image intensity at point (x,z), i, j are the transmit/receive indices of the phased array elements, s_{ij} is the full matrix of analytic time domain signal transmitted from element i and received on element j. τ is the arrival time at each focal point, which in this paper is calculated either by a single straight line solution, or using DA ray tracing; in the case of the single straight line approximation, $\tau = \sqrt{x^2 + z^2}/v_g$, where v_g is the group velocity.

RESULTS

Arrival time accuracy

To demonstrate how the different parameters affect the accuracy of the DA solution, the average error throughout the sample is used. While this loses some valuable information about the spatial distribution of the error, it provides a global heuristic with which to optimise parameters; more specific optimisation can be obtained on a case by case basis. Arrival times are interpolated using Matlab's built-in `scatteredInterpolant` function, with default linear interpolation, for both FEA and DA results. The error is the difference between the DA and FEA results.

Figure 3 shows the error as a function of the normalised maximum connection distance,

$$k_{\text{hop}} = \frac{r_{\text{hop}}}{r_{\text{min}}} \tag{3}$$

wher r_{hop} is the maximum connection distance, and r_{min} is a characteristic length of the vertex distribution. In the case of the regular sampling grids, this is the lattice parameter; in the case of Poisson disc sampling this is the minimum point separation.

The result clearly shows a minimum for all cases; this is best compromise between the homogenisation effect of long hops and the poor angular resolution of shorter hops. There is little advantage in using any distribution over any other, except the square grid shows a slightly poorer accuracy.

In this case an $k_{\text{hop}} \approx 5$ is the optimum value. However, this may well change with material properties, and is a point for further investigation.

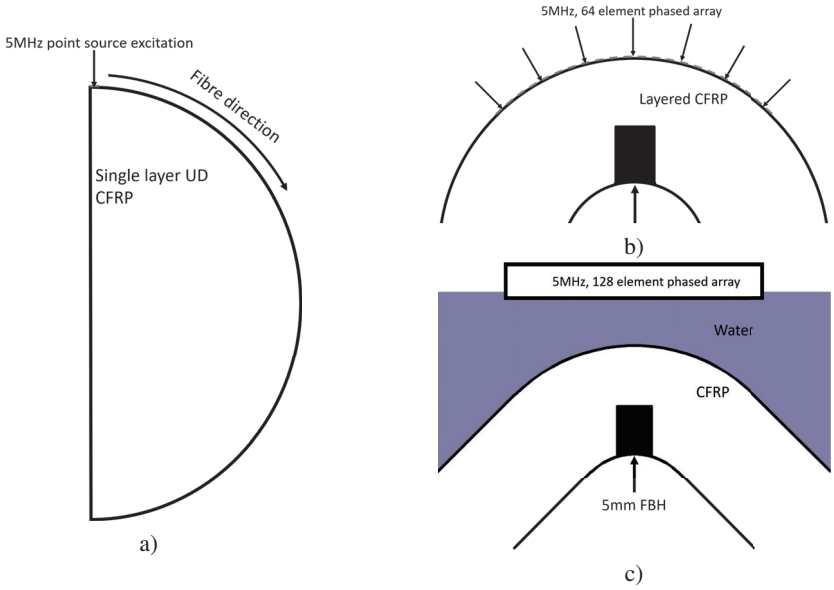

FIGURE 2. a) Finite element model for arrival time accuracy calculations. b) Finite element FMC calculation (pipe cross section). c) Experimental setup (corner section).

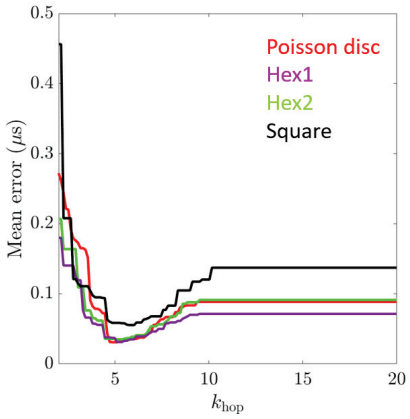

FIGURE 3. Mean error in the specimen

TFM imaging

Figure 4 shows contact TFM images calculated using simulated data, normalised to the maximum value. The straight line focal law (Fig.4a) provides results which are difficult to interpret. The corners of the hole are visible, but the signal from the top surface of the hole is spread out, making characterising the defect almost impossible. The back wall reflection corresponding to the concave surface either side of the defect opening is also slightly incorrectly placed.

Applying DA modification (Fig.4b))to the focal law results in a much more visible defect. The structural noise is more localised towards the surface of the specimen. The back wall signals are also more accurately positioned. In both straight line and DA cases, there appears to be secondary echoes of the back wall and defect (in the DA case); the exact physical cause of these are as yet unknown.

Figure 5 shows immersion TFM images for the composite corner specimen, with a 5 mm flat bottomed hole. Each image is displayed with a 30 dB dynamic range relative to the maximum signal. Left to right show straight line focal law and DA focal law respectively. Top to bottom show 5 MHz and 2 MHz filter frequencies respectively.

Examining the 5 MHz filtered case, Fig.5a),b), the peak signal is greater for the DA modified case. However, a

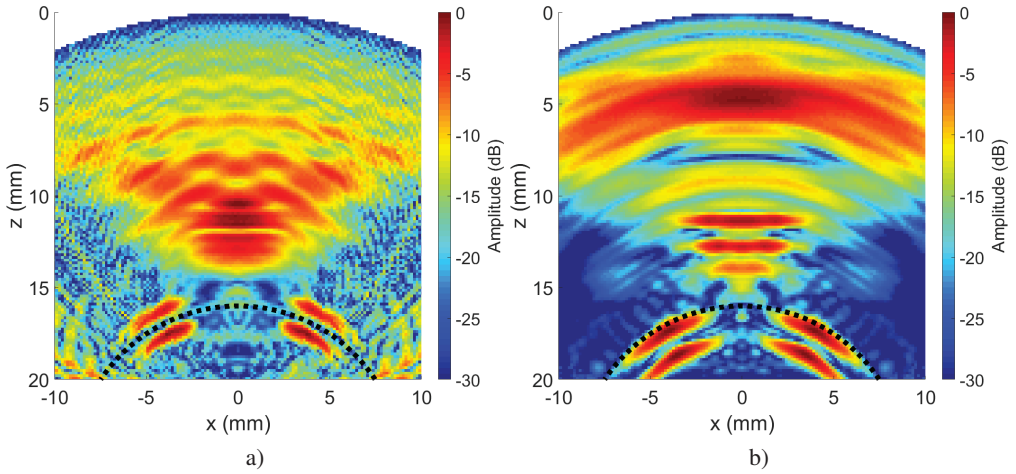

FIGURE 4. TFM on simulated contact FMC, filtered at 2MHz. a) Straight line focal law b) DA modified focal law. The back wall is shown as a black dashed line.

greater level of coherent noise is also present near the defect depth; this is likely due to the ply responses being summed in more accurate locations. While with refinement, this may be useful for detecting ply waviness or interfacial defects, for imaging the defect in this case it is a hindrance.

In the 2 MHz case, Fig.5d), the defect signal is much clearer. The ply response is greater near the surface, but unlikely to be useful for detection of ply interfaces due to the small thickness of the plies. This coherent noise is somewhat similar to that seen in the simulated data (Fig.4b)). There are some differences however; moving circumferentially away from the centre of the array, the noise signal is less than in the FE results. This is because the outer elements of the array provide a greater amount of signal in the simulated data due to the normal incidence and perfect contact assumption. Much of the energy of these outer elements is lost to specular reflection in the immersion case.

Figure 6a) shows the estimated signal-to-noise ratio for both methods as a function of the filter centre frequency. The noise was estimated by calculating the RMS of the signal present in the immediate vicinity of the defect, in an area approximately 5 mm by 2 mm directly above the defect. It should be noted that this is valid only as a rough estimate, as there is no accurate way to measure the noise concurrent with the defect location.

There is a significant improvement at lower frequencies when using the DA modified focal law. As the frequencies increase, the ply resonance is approached; single straight line approximations spread the ply signals out more, reducing the amplitude of the structural noise at this frequency. DA by comparison increases the level of structural noise in this region. At 5 Mhz, the SNR is worse for the DA case than the straight line case; it is posited that this is due to the more accurate arrival times for the ply reflections. These more accurate arrival times mean that the signal will be more spatially concentrated, causing greater coherent noise levels in the final image.

Figure 6b) shows the 6dB sizes calculated with straight line and DA modified focal laws. This is calculated by measuring the width at the points where the signal has dropped by 6 dB from the peak of the defect.

It is clear that the DA modified focal law greatly improves the sizing accuracy for defects of this size, even at the higher frequency when SNR is reduced.

CONCLUSIONS

In this work, Dijkstra's algorithm has been demonstrated as a potential method for improving imaging of defects in curved composite components. The accuracy has been demonstrated to be strongly dependent on the allowed transit distance between vertices. Finite element models have shown that Dijkstra's algorithm vastly improved the detectability of defects in simulated data. Experimentally, improved signal-to-noise and sizing estimates have been found for large defects.

Future study into the behaviour of the optimum k_{hop}, specifically how spatial error distribution is affected, and it's dependence on anisotropy level, may be useful. Investigating a larger range of defect sizes would verify the usefulness of DA further; it is possible that small defects which are normally invisible due to poor signal reconstruction

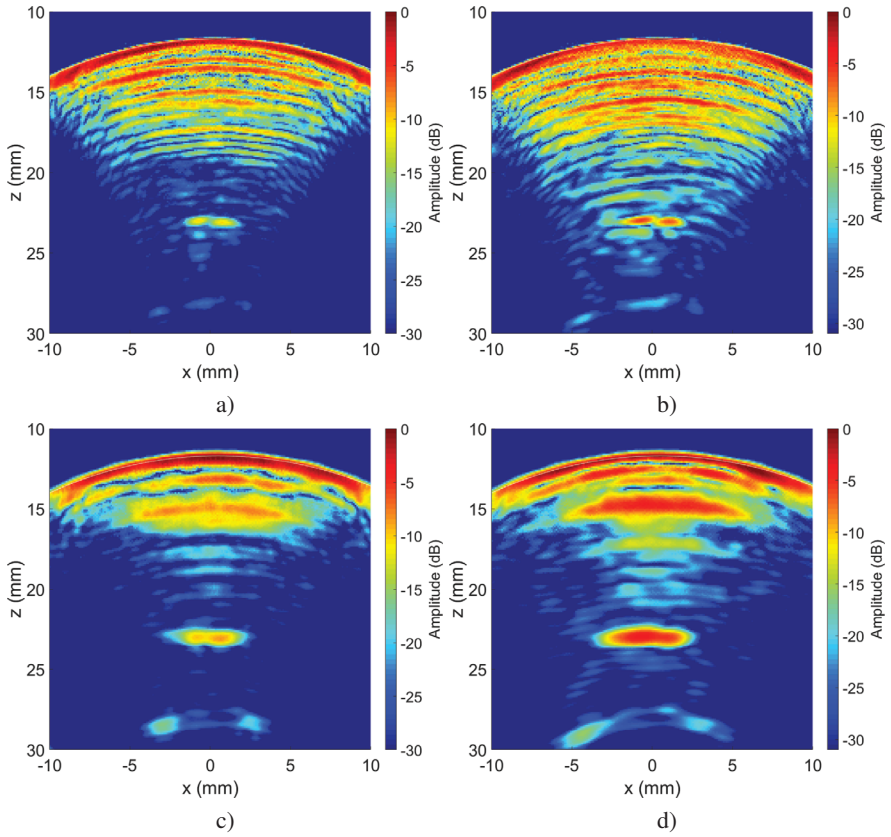

FIGURE 5. Experimental TFM images. a) 5 MHz filter, unmodified focal law, b) 5 MHz filter, DA modified focal law, c) 2 MHz filter, unmodified focal law, d) 2 MHz filter, DA modified focal law

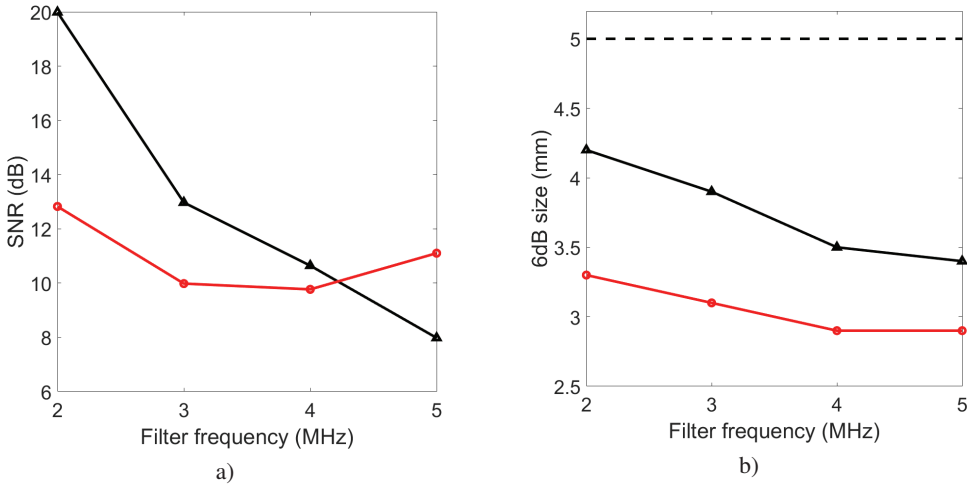

FIGURE 6. Comparison of a) signal-to-noise and b) sizing using straight line focal law (red, circles) and DA modified focal law (black, triangles).

may now become visible.

It should also be possible to reduce coherent noise further by angle limiting the aperture [7, 8]; the angle from Dijkstra's algorithm could be used to further enhance this process.

ACKNOWLEDGEMENTS

The authors would like to thank the Engineering and Physical Sciences Research Council (EPSRC) for funding this work through the Centre for Doctoral Training in Advanced Composite for Innovation and Science, grant number EP/L016028/1.

REFERENCES

[1] S. R. Kolkoori, M. U. Rahman, P. K. Chinta, M. Ktreutzbruck, M. Rethmeier, and J. Prager, "Ultrasonic field profile evaluation in acoustically inhomogeneous anisotropic materials using 2D ray tracing model: Numerical and experimental comparison", *Ultrasonics* **53**, 396–411 (2013).

[2] V. Farra, "Ray tracing in complex media", *Journal of Applied Geophysics* **30**, 55–73 (1993).

[3] T. J. Moser, "Shortest path calculation of seismic rays", *Geophysics* **56**, 59–67 (1991).

[4] O. Nowers, D. J. Duxbury, J. Zhang, and B. W. Drinkwater, "Novel ray-tracing algorithms in NDE: Application of Dijkstra and A* algorithms to the inspection of an anisotropic weld", *NDT and E International* **61**, 58–66 (2014).

[5] E. W. Dijkstra, "A note on two problems in connection with graphs", *Numerische Mathematik* **1**, 269–271 (1959).

[6] P. Huthwaite, "Accelerated finite element elastodynamic simulations using the GPU", *Journal of Computational Physics* **257**, 687–707 (2014).

[7] Y. Humeida, V. J. Pinfield, R. E. Challis, P. D. Wilcox, and C. Li, "Simulation of ultrasonic array imaging of composite materials with defects", *IEEE transactions on ultrasonics, ferro- electrics, and frequency control* **60**, 1935–48 (2013).

[8] C. Li, D. Pain, P. D. Wilcox, and B. W. Drinkwater, "Imaging composite materials using ultrasonic arrays", *NDT & E International* **53**, 8–17 (2013).